

# Supporting Information

## Identification of the Intrinsic Dielectric Properties of Metal Single Atoms for Electromagnetic Wave Absorption

Xinci Zhang<sup>1</sup>, Yanan Shi<sup>1</sup>, Jia Xu<sup>1</sup>, Qiuyun Ouyang<sup>1</sup>, Xiao Zhang<sup>1,\*</sup>, Chunling Zhu<sup>2,\*</sup>, Xiaoli Zhang<sup>3</sup> and Yujin Chen<sup>1,2,3\*</sup>

<sup>1</sup> Key Laboratory of In-Fiber Integrated Optics, College of Physics and Optoelectronic Engineering, Harbin Engineering University, Harbin 150001, China

<sup>2</sup> College of Materials Science and Chemical Engineering, Harbin Engineering University, Harbin 150001, China

<sup>3</sup> School of Materials Science and Engineering, Zhengzhou University, Zhengzhou 450001, China

\* Corresponding authors.

E-mail: zhangxiaochu@hrbeu.edu.cn; zhuchunling@hrbeu.edu.cn;  
chenyujin@hrbeu.edu.cn

**Material characterization:**

The morphology and size of the synthesized samples were characterized via XRD using an X'Pert Pro diffractometer with Cu K $\alpha$  radiation ( $\lambda = 1.5418 \text{ \AA}$ ). The samples were scanned from  $10^\circ$  to  $70^\circ$  at a scanning rate of  $5^\circ/\text{min}$ . Raman spectroscopy was conducted to characterize the extent of disorder in the carbon materials using a Lab RAM Aramis micro Raman spectrometer with an excitation wavelength of 488 nm and a spot size of  $2 \text{ }\mu\text{m}$ . The morphology of all samples was observed using a Hitachi SU8000 scanning electron microscope at an accelerating voltage of 5–20 kV. The samples were pasted onto conductive tapes for SEM observations. TEM images were acquired using a JEM-2100 transmission electron microscope operating at a voltage of 200 kV. SEM-EDX analyses were performed to confirm the elemental contents of the samples. The ethanol solution containing the sample was treated using ultrasounds for 5 min, and the solution was then dripped onto a copper grid for TEM observations. XPS measurements were carried out using an X-ray photoelectron spectrometer (K-Alpha, Thermofisher Scientific Company) with Al K $\alpha$  radiation generated at 12 kV and 150 W. The binding energies of all samples were determined using the carbon C 1s peak (284.6 eV) as a reference. A Micromeritics ASAP 2010 micropore size analyzer was used to measure the specific surface area of the sample from the linear portion of the BET plots ( $P/P_0 = 0.01\text{--}0.10$ ) at 77 K. Approximately 0.2 g of catalyst was placed in a quartz tube. ICP-OES measurements were performed to determine the metal contents in the catalysts. The conductivity of the samples was determined using an X3 Hall Effect Test System (Semishare International Limited).

### XAFS measurements:

The obtained XAFS data was processed using the Athena software (version 0.9.26) for background, pre-edge line, and post-edge line calibrations. Then, FT fitting was carried out with the Artemis software (version 0.9.26). A  $k^3$  weighting, a  $k$ -range of 2–5  $\text{\AA}^{-1}$ , and an  $R$ -range of 1–4  $\text{\AA}$  were used for the fitting of the Mn sample. The coordination number, bond length, Debye–Waller factor, and  $E_0$  shift ( $CN$ ,  $R$ ,  $\sigma^2$ ,  $\Delta E_0$ ) were fitted without being fixed, constrained, or correlated. For the WT analysis, the  $\chi(k)$  value exported from Athena was imported into the Hama Fortran code. The parameters were as follows:  $R$ -range, 1–4  $\text{\AA}$ ;  $k$ -range,  $\sim 0$ –13  $\text{\AA}^{-1}$  for standers (0–6  $\text{\AA}^{-1}$  for the Mn sample);  $k$ -weight, 2. The Morlet function with  $\kappa = 10$  and  $\sigma = 1$  was used as the mother wavelet to provide the overall distribution.

### Figures and Tables

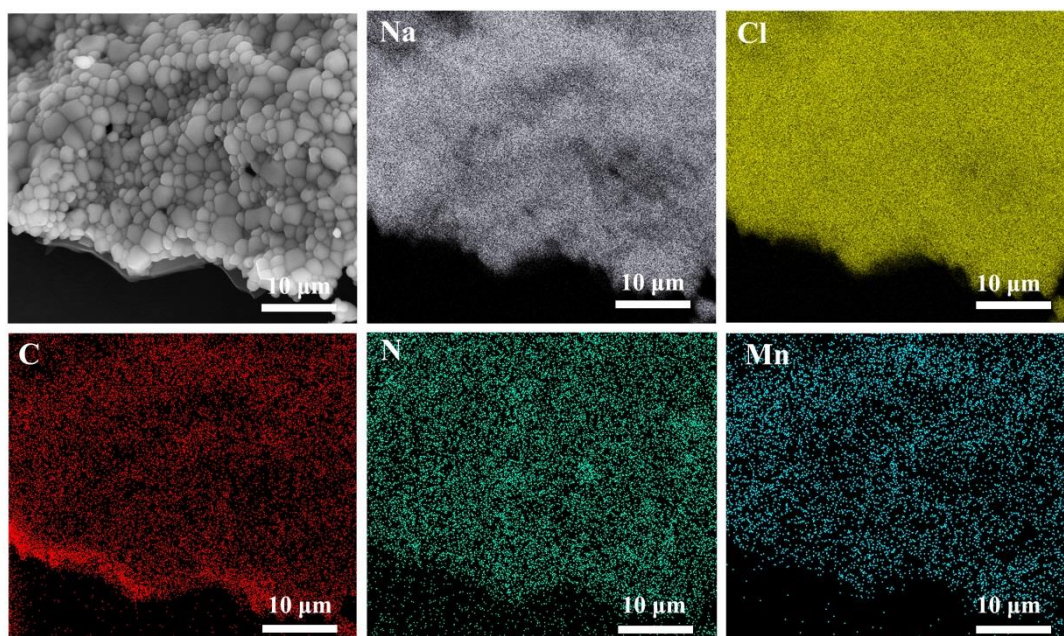


**Fig. S1** SEM image and EDX mapping of the 3D Mn–NC precursor after freeze-drying process.

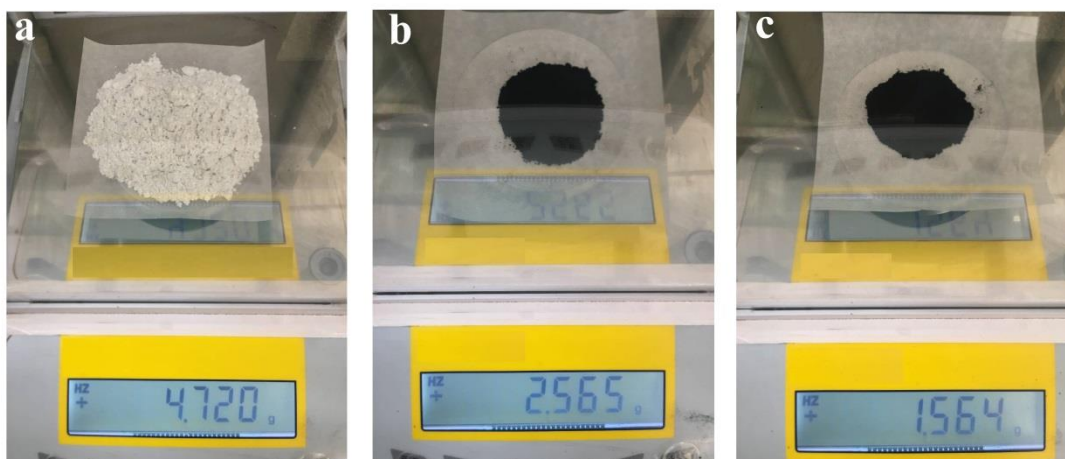


**Fig. S2** Photos of 3D Mn-NC production in each batch. **a** The precursor after freeze-drying process. **b** The sample after carbonized at 800°C. **c** The finally product of 3D Mn-NC.

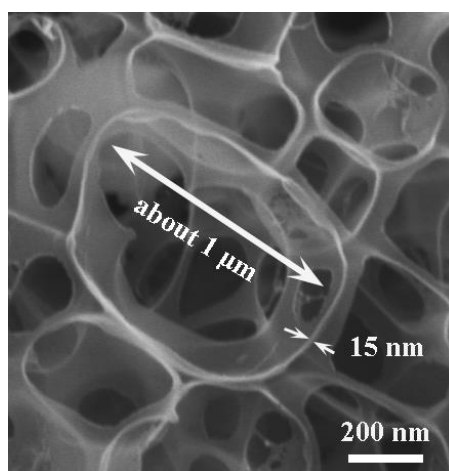


**Fig. S3** SEM images of the 3D Mn-NC.

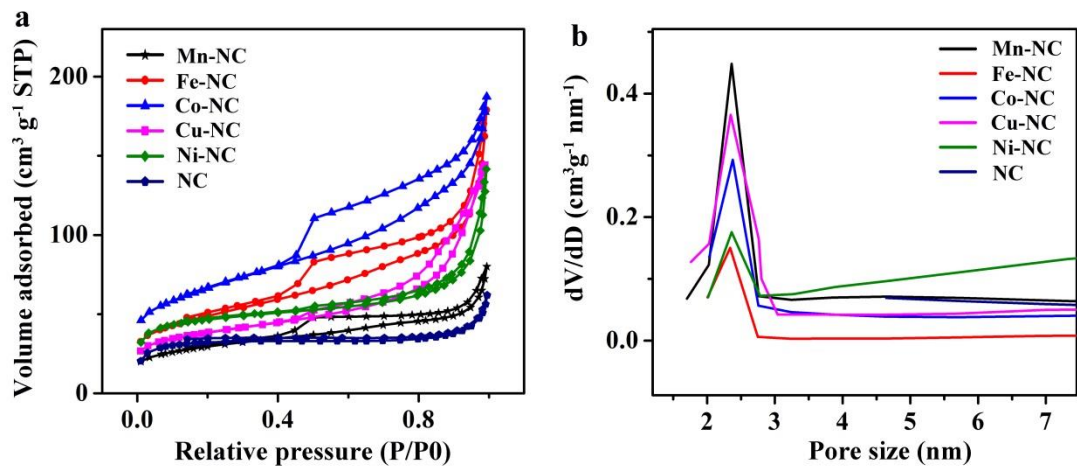


**Fig. S4** **a** N<sub>2</sub> adsorption–desorption isotherms and **b** pore-size distribution of different samples.

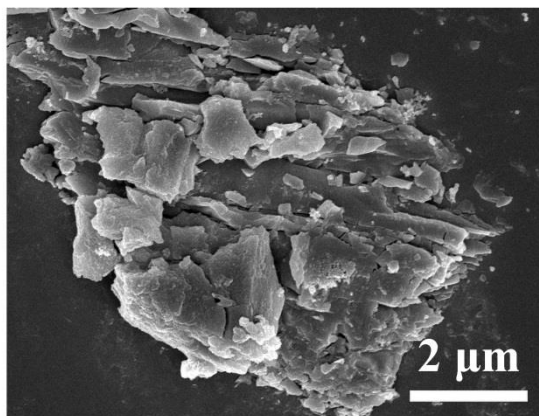


**Fig. S5** SEM images of the Mn-N<sub>x</sub>C-w.

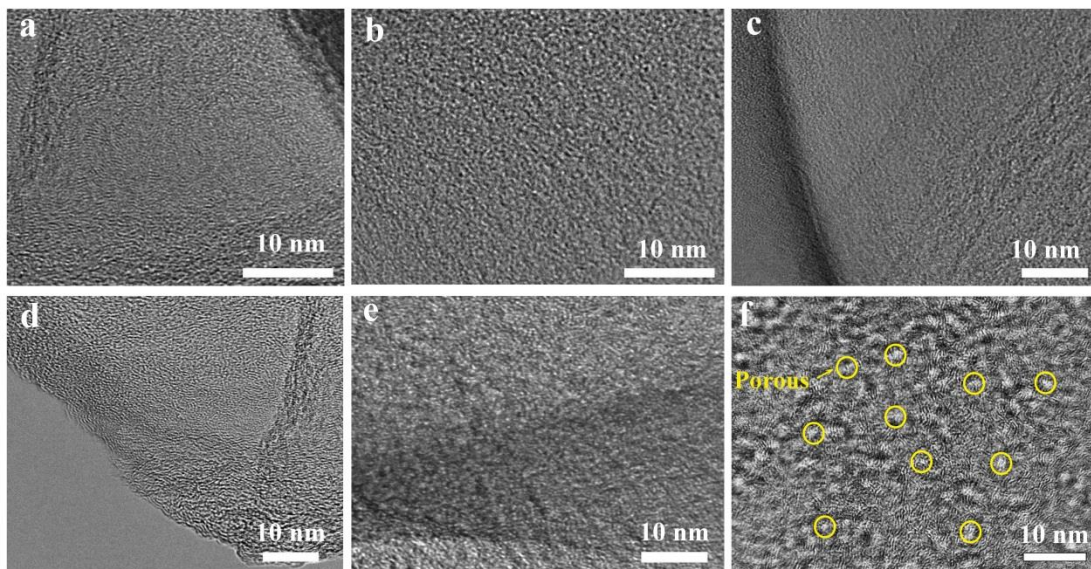


**Fig. S6** HRTEM images of **a** 3D NC, **b** 3D Fe-NC, **c** 3D Cu-NC, **d** 3D Ni-NC and **e** 3D Co-NC, and **f** 3D Mn-NC.

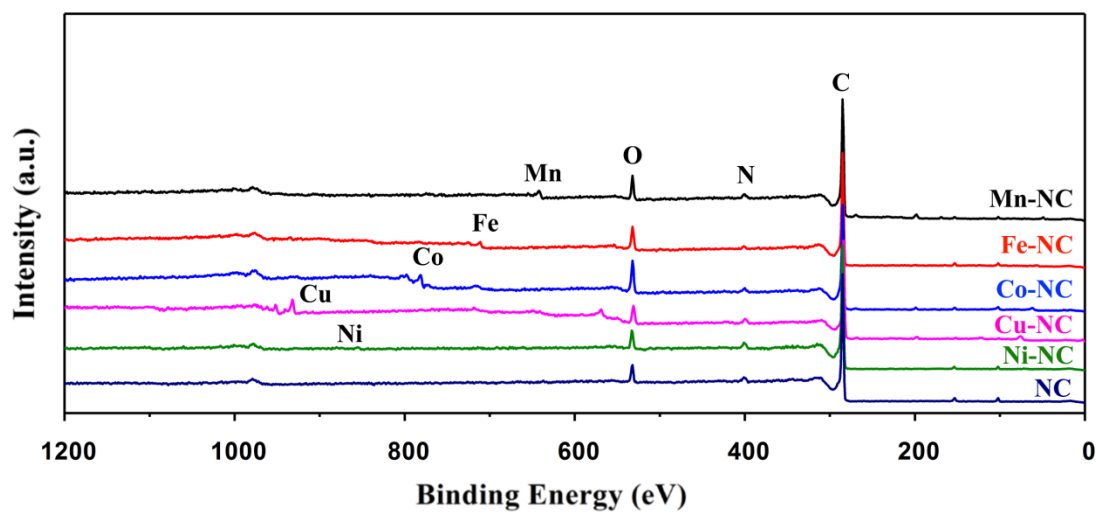


**Fig. S7** X-ray photoelectron spectroscopy (XPS) patterns of 3D NC, 3D Ni-NC, 3D Cu-NC, 3D Co-NC, 3D Fe-NC, and 3D Mn-NC.

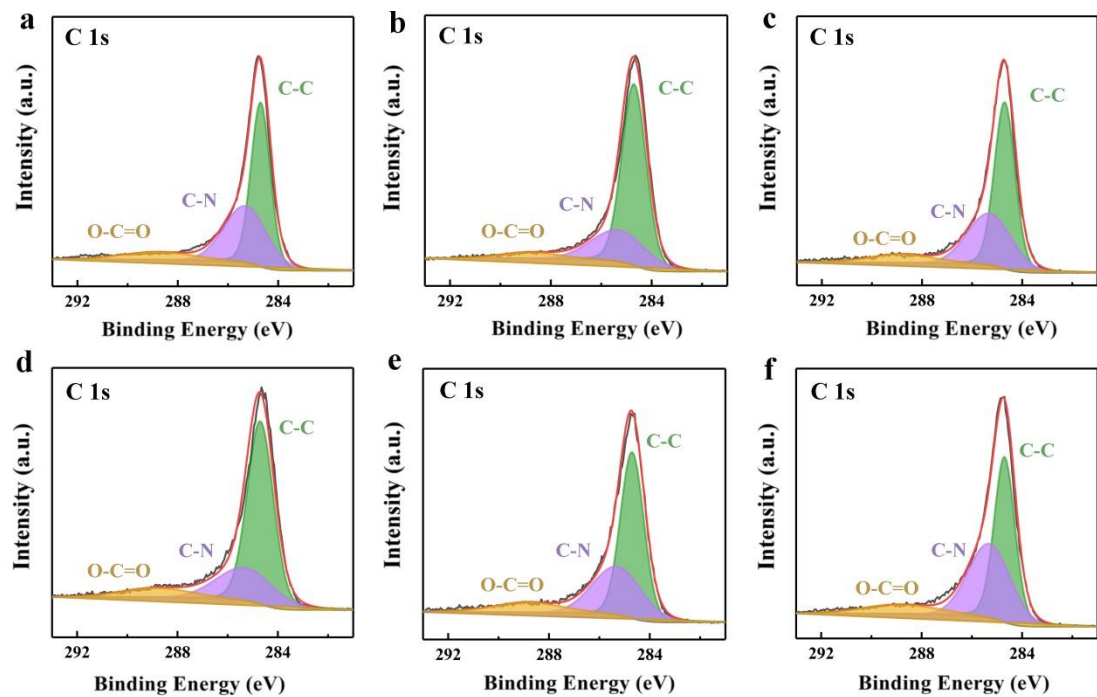


**Fig. S8** C 1s XPS spectra of **a** 3D NC, **b** 3D Mn-NC, **c** 3D Fe-NC, **d** 3D Co-NC, **e** 3D Cu-NC, and **f** 3D Ni-NC.

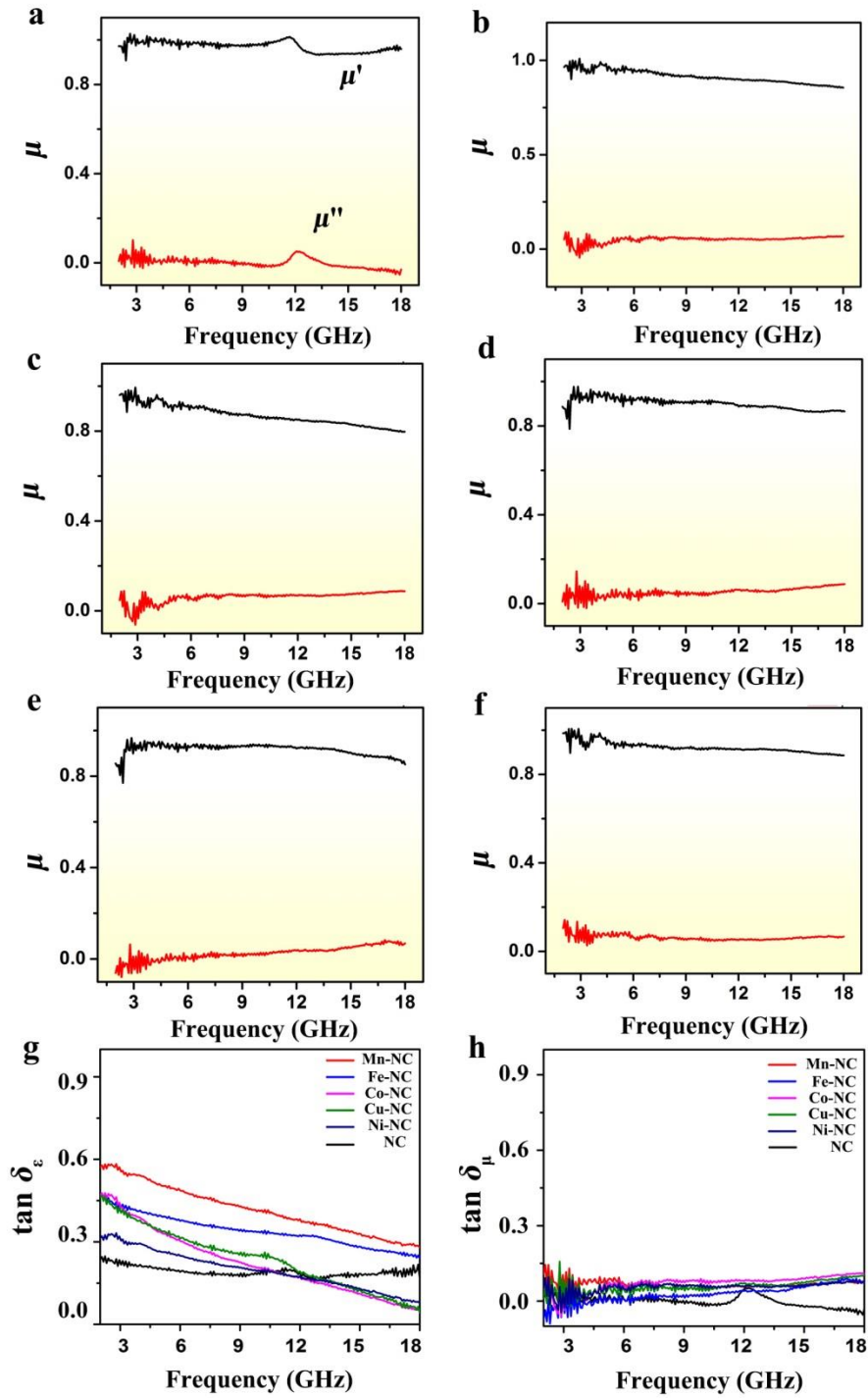


**Fig. S9** The relative real parts, imaginary parts of the complex permeability of **a** 3D NC, **b** 3D Ni-NC, **c** 3D Cu-NC, **d** 3D Co-NC, **e** 3D Fe-NC, and **f** 3D Mn-NC. **g-h** Dielectric loss tangent and magnetic loss tangent of the samples.

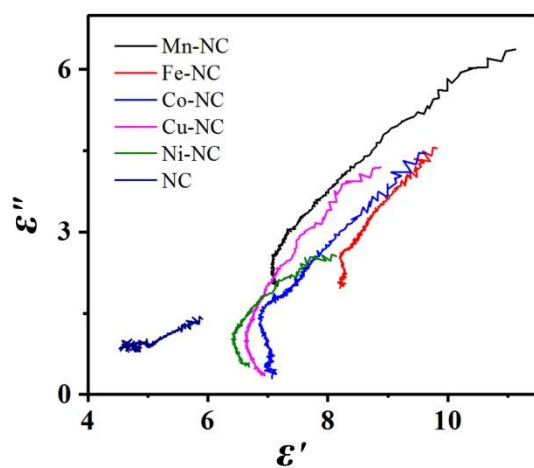


**Fig. S10** Cole–Cole plots of all the samples.

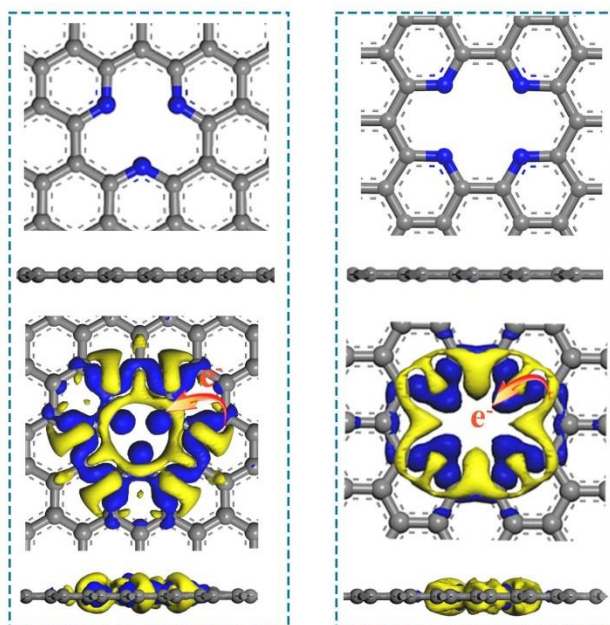


**Fig. S11** Calculated charge density difference of the different type N-doped sites in a single graphitic plane.

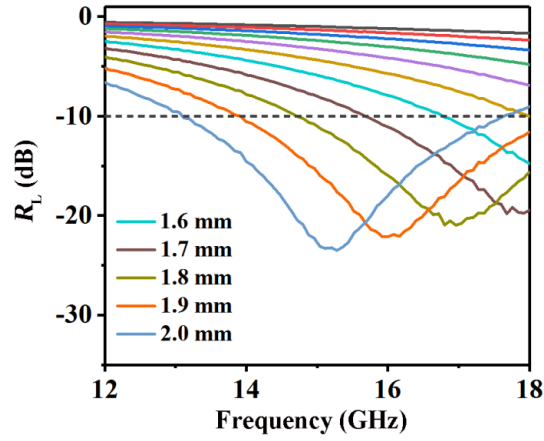


**Fig. S12** Reflection loss curves of 3D Mn-NC at the thickness  $< 2.0$  mm.

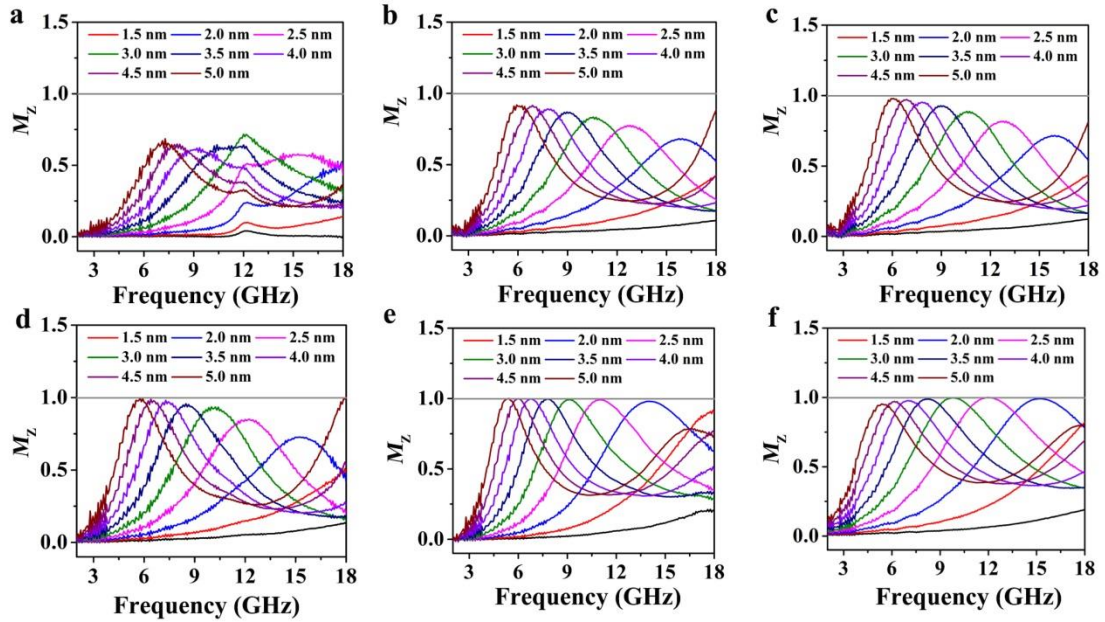


**Fig. S13** The degree of impedance matching of **a** 3D NC, **b** 3D Ni-NC, **c** 3D Cu-NC, **d** 3D Co-NC, **e** 3D Fe-NC, and **f** 3D Mn-NC.

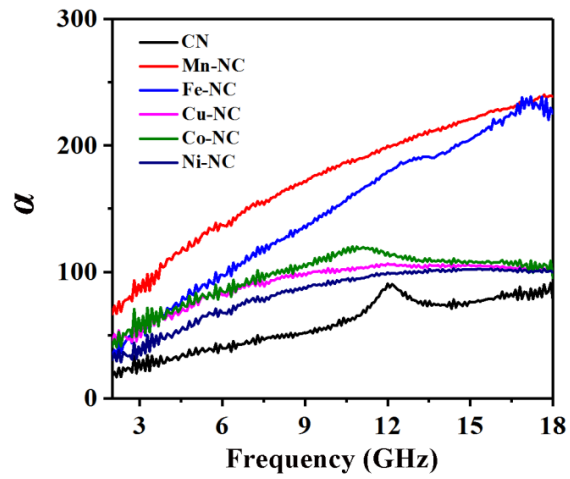


**Fig. S14** The  $\alpha$ - $f$  curves of all the samples.

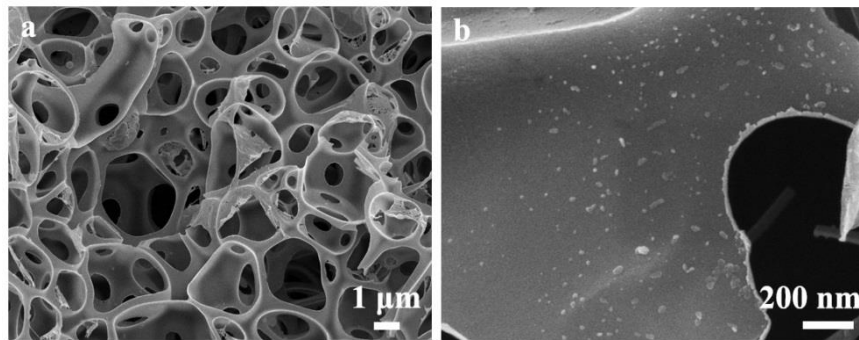


**Fig. S15** SEM images of the 3D Mn NPs-NC.

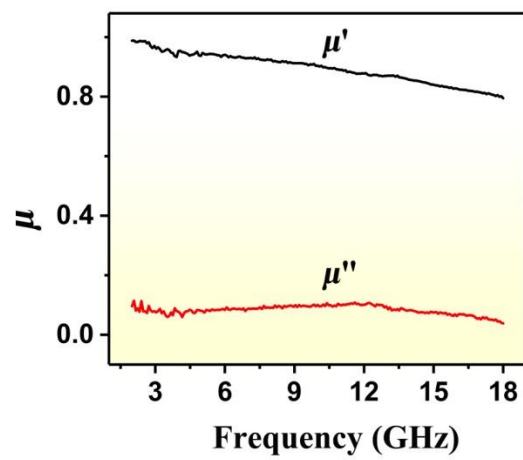


**Fig. S16** Frequency dependence of  $\mu_r$  of 3D Mn NPs-NC.

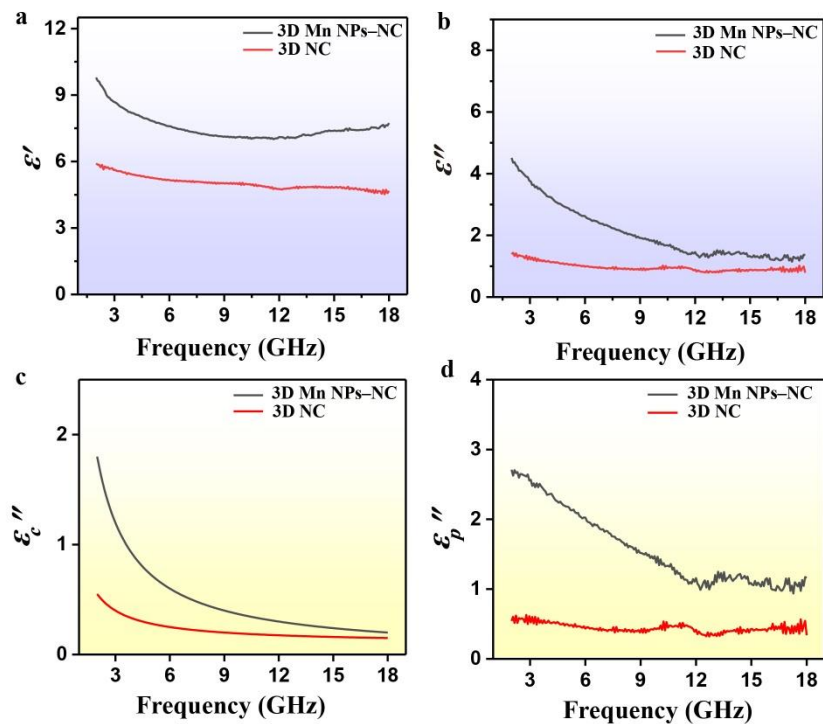


**Fig. S17 a–d** Frequency dependence of  $\epsilon'$ ,  $\epsilon''$ ,  $\epsilon_c''$  and  $\epsilon_p''$  of 3D Mn NPs–NC and 3D NC.

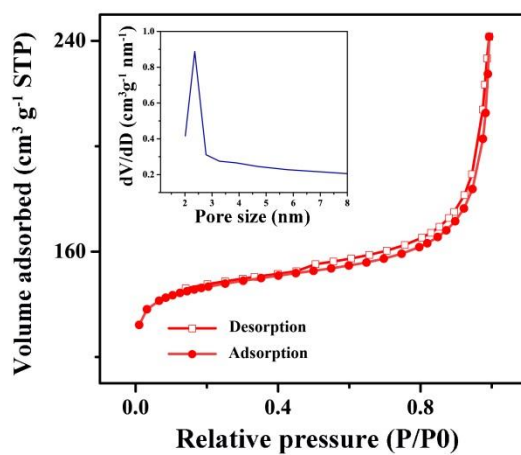


**Fig. S18**  $N_2$  adsorption–desorption isotherms of the 3D Mn NPs–NC.

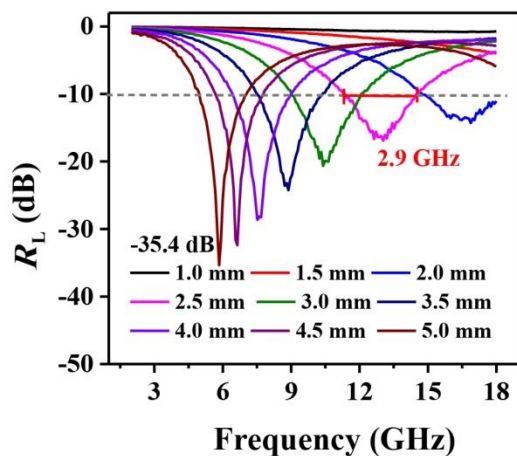


Fig. S19 Reflection loss curves of the 3D Mn NPs-NC.

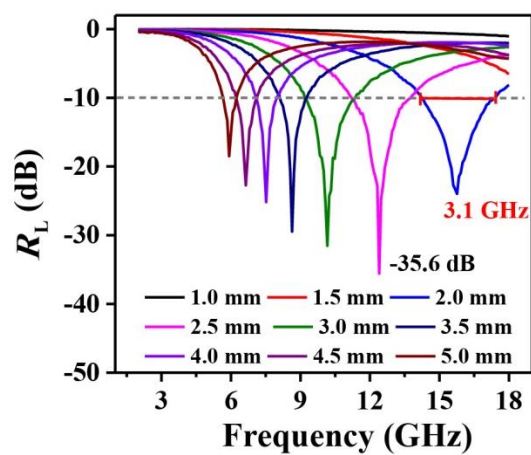


Fig. S20 Reflection loss curves of the Mn- $N_x$ C-w.

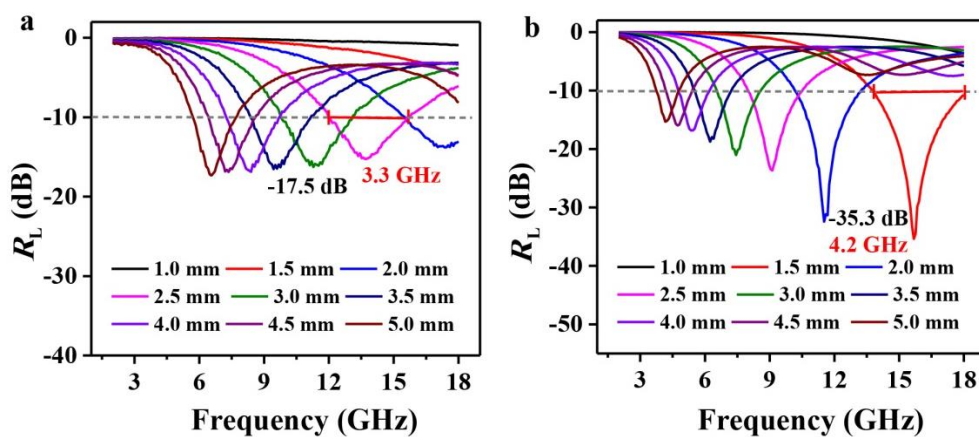
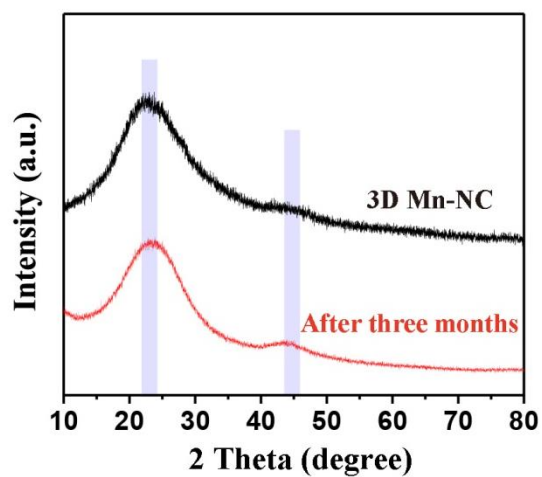
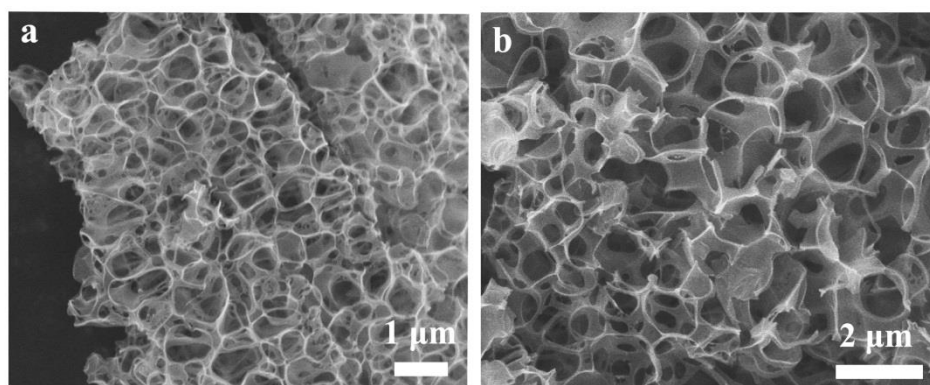


Fig. S21 Reflection loss curves of the 3D Mn-NC with a filler loading of a) 5 wt.%, b) 15 wt.%.



**Fig. S22** XRD patterns of the 3D Mn-NC and the 3D Mn-NC sample stored for three months.



**Fig. S23** SEM images of **a** 3D Mn-NC and **b** 3D Mn-NC sample stored for three months.

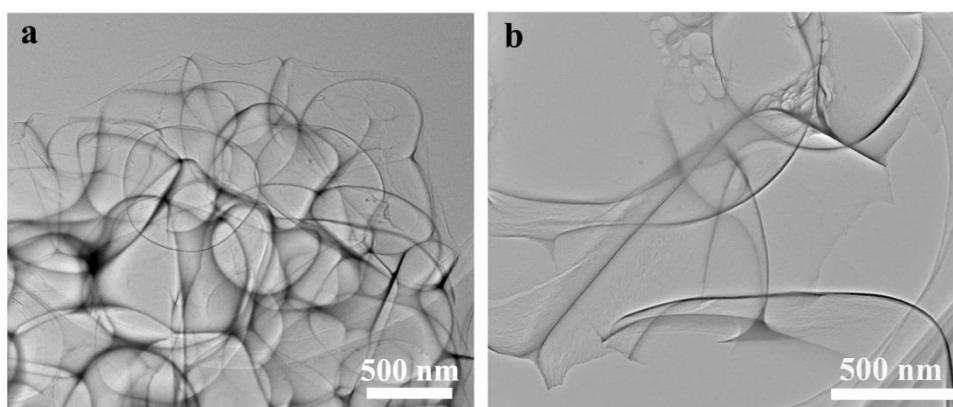


**Fig. S24** TEM images of **a** 3D Mn-NC and **b** 3D Mn-NC sample stored for three months.

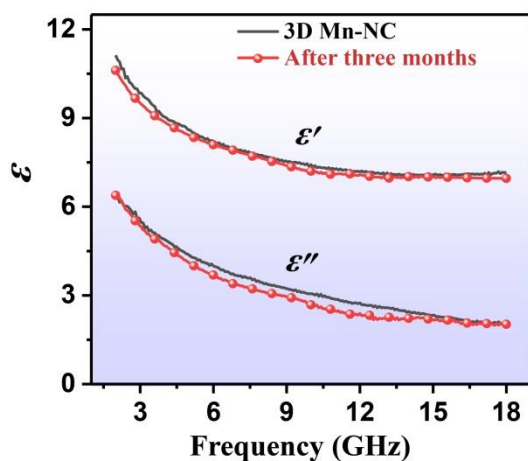


**Fig. S25** Frequency dependence of  $\epsilon_r$  of the 3D Mn-NC and the 3D Mn-NC sample stored for three months.

**Table S1** BET specific surface area and pore size for all the samples.

	CN	Mn-NC	Fe-NC	Co-NC	Cu-NC	Ni-NC
BET surface areas ( $\text{m}^2/\text{g}$ )	550	634	607	599	580	570
Pore size (nm)	2.35	2.32	2.37	2.35	2.33	2.35

**Table S2** Content of nitrogen species in the different samples.

	CN	Mn-NC	Fe-NC	Co-NC	Cu-NC	Ni-NC
N (at.%)	2.1	3.6	3.2	3.0	2.6	2.4

**Table S3** ICP-AES results of all the samples.

	Mn-NC	Fe-NC	Co-NC	Cu-NC	Ni-NC
Metal (wt.%)	1.80	1.40	1.38	1.17	1.12

**Table S4** EXAFS fitting parameters at the Mn K-edge various samples ( $S_0^2=0.11$ ).

Sample	Path	C.N.	R (Å)	$\sigma^2 \times 10^3$ (Å <sup>2</sup> )	$\Delta E$ (eV)	R factor
Mn foil	Mn-Mn	12*	2.66±0.01	7.2±1.6	4.0±2.4	0.011
MnO	Mn-O	5.5±1.0	2.19±0.01	5.3±1.8	3.0±1.8	0.007
	Mn-Mn	16.0±2.3	3.14±0.01	10.0±1.2	1.9±1.2	
Mn <sub>2</sub> O <sub>3</sub>	Mn-O	5.1±0.9	1.91±0.01	5.8±1.8	-4.0±2.3	0.09
	Mn-Mn	12.7±2.3	3.15±0.01	11.3±1.4	5.7±1.2	
Mn-NC	Mn-N	3.8±1.9	2.16±0.04	7.6±8.8	8.9±2.7	0.016

<sup>a</sup>C.N.: coordination numbers; <sup>b</sup>R: bond distance; <sup>c</sup> $\sigma^2$ : Debye-Waller factors; <sup>d</sup>  $\Delta E$ : the inner potential correction. R factor: goodness of fit. \* The experimental EXAFS fit of metal foil by fixing CN as the known crystallographic value.

**Table S5** Electrical conductivity for all the samples.

	Mn-NC	Fe-NC	Co-NC	Cu-NC	Ni-NC	NC
$\sigma$ (S m <sup>-1</sup> )	4.40	4.16	4.02	3.96	3.87	1.01

**Table S6** Mulliken charge (local of N<sub>4</sub>C and M-N<sub>4</sub>C structure) for all the samples.

	CN	Mn-NC	Fe-NC	Co-NC	Cu-NC	Ni-NC
C	0.18	0.11	0.11	0.11	0.11	0.11
N	-0.33	-0.43	-0.47	-0.46	-0.49	-0.45
Metal		1.17	1.23	1.18	1.42	1.20

**Table S7** Comparison of the EMW absorption performance of the previously reported carbon-based absorbers.

Absorbers	$R_{L, \min}$ (dB)	Optimum thickness (mm)	Filler loading (wt. %)	$SRL_l$ (dB·mg <sup>-1</sup> )	$SRL_{lt}$ (dB·mm <sup>-1</sup> ·mg <sup>-1</sup> )	Ref.
Mn-NC	-46.2	2	10	-4.62	-2.31	This work
GO-CNT-Fe <sub>3</sub> O <sub>4</sub>	-37.25	5	30	-1.24	-0.25	[s1]
FeCo-CNT	-46.5	1.7	50	-0.93	-0.55	[s2]
C-Fe <sub>2</sub> O <sub>3</sub> -Fe <sub>3</sub> C- Fe-CNT	-42.6	3.5	20	-2.13	-0.61	[s3]
Co-CNT-G	-65.6	2.19	30	-2.18	-0.99	[s4]
Fe <sub>3</sub> O <sub>4</sub> -CNT-	-50.9	2.5	25	-2.03	-0.81	[s5]
Carbon fibers						
Fe <sub>3</sub> O <sub>4</sub> -CNT	-43	1.5	30	-1.43	-0.95	[s6]

Ferrite/Co/porous carbon	-47.3	2.5	70	-0.68	-0.27	[s7]
Co–C	-62.12	2.4	30	-2.07	-0.86	[s8]
Co@C microspheres	-68.7	1.65	70	-0.98	-0.59	[s9]
CNT@TiO <sub>2</sub> sponges	-31.8	2.0	30	-1.06	-0.53	[s10]
FeCo/graphene hybrids	-40.2	2.5	50	-0.80	-0.32	[s11]
CoFe@C	-43.5	2.5	50	-0.87	-0.34	[s12]

## References

- [s1] L. Wang, X. Jia, Y. Li, F. Yang, L. Zhang et al., Synthesis and microwave absorption property of flexible magnetic film based on graphene oxide/carbon nanotubes and Fe<sub>3</sub>O<sub>4</sub> nanoparticles. *J. Mater. Chem. A* **2**, 14940–14946 (2014). <https://doi.org/10.1039/C4TA02815E>
- [s2] B. Yang, Y. Wu, X. Li, R. Yu, Surface-oxidized FeCo/carbon nanotubes nanorods for lightweight and efficient microwave absorbers. *Materials and Design* **136**, 13–22 (2017). <https://doi.org/10.1016/j.matdes.2017.09.055>
- [s3] B. Zhong, C. Wang, G. Wen, Y. Yu, L. Xia, Facile fabrication of boron and nitrogen co-doped carbon@Fe<sub>2</sub>O<sub>3</sub>/Fe<sub>3</sub>C/Fe nanoparticle decorated carbon nanotubes three-dimensional structure with excellent microwave absorption properties. *Compos.*

Part B-Eng. **132**, 141–150 (2018).

<http://dx.doi.org/10.1016/j.compositesb.2017.09.001>

[s4] X. Qi, Q. Hu, H. Cai, R. Xie, Z. Bai et al., Heteronanostructured Co@carbon nanotubes-graphene ternary hybrids: synthesis, electromagnetic and excellent microwave absorption properties. *Sci. Rep.* **6**, 37972 (2016).

<https://doi.org/10.1038/srep37972>

[s5] J. Qiu, T. Qiu, Fabrication and microwave absorption properties of magnetite nanoparticle–carbon nanotube–hollow carbon fiber composites. *Carbon* **81**, 20–28 (2015). <http://dx.doi.org/10.1016/j.carbon.2014.09.011>

[s6] N. Li, G. Huang, Y. Li, H. Xiao, Q. Feng et al., Enhanced microwave absorption performance of coated carbon nanotubes by optimizing the Fe<sub>3</sub>O<sub>4</sub> nanocoating structure. *ACS Appl. Mater. Interfaces* **9**, 2973–2983 (2017).

<https://doi.org/10.1021/acsami.6b13142>

[s7] L. Wang, Y. Guan, X. Qiu, H. Zhu, S. Pan et al., Efficient ferrite/Co/porous carbon microwave absorbing material based on ferrite@metal–organic framework. *Chem. Eng. J.* **326**, 945–955 (2017). <http://dx.doi.org/10.1016/j.cej.2017.06.006>

[s8] K. Wang, Y. Chen, R. Tian, H. Li, Y. Zhou et al., Porous Co–C core–shell nanocomposites derived from Co-MOF-74 with enhanced electromagnetic wave absorption performance. *ACS Appl. Mater. Interfaces* **10**, 11333–11342 (2018).

<https://doi.org/10.1021/acsami.8b00965>

[s9] D. Ding, Y. Wang, X. Li, R. Qiang, P. Xu et al., Rational design of core-shell Co@C microspheres for high-performance microwave absorption. *Carbon* **111**,

722–732 (2017). <http://dx.doi.org/10.1016/j.carbon.2016.10.059>

[s10] C. Mo, R. Yang, D. Lu, L. Yang, Q. Hu et al., Lightweight, three-dimensional carbon nanotube@TiO<sub>2</sub> sponge with enhanced microwave absorption performance. *Carbon* **144**, 433–439 (2019). <https://doi.org/10.1016/j.carbon.2018.12.064>

[s11] X. Li, J. Feng, Y. Du, J. Bai, H. Fan et al., One-pot synthesis of CoFe<sub>2</sub>O<sub>4</sub>/graphene oxide hybrids and their conversion into FeCo/graphene hybrids for lightweight and highly efficient microwave absorber. *J. Mater. Chem. A* **3**, 5535–5546 (2015). <https://doi.org/10.1039/C4TA05718J>

[s12] X. Zeng, B. Yang, L. Zhu, H. Yang, R. Yu, Structure evolution of prussian blue analogues to CoFe@C core–shell nanocomposites with good microwave absorbing performances. *RSC Adv.* **6**, 105644–105652 (2016). <https://doi.org/10.1039/C6RA18928H>